Beyond the molecular movie: Dynamics of bands and bonds during a photoinduced phase transition

C. W. Nicholson[1]*†, A. Lücke[2], W. G. Schmidt[2], M. Puppin[1], L. Rettig[1], R. Ernstorfer[1], M. Wolf[1]*

Ultrafast nonequilibrium dynamics offer a route to study the microscopic interactions that govern macroscopic behavior. In particular, photoinduced phase transitions (PIPTs) in solids provide a test case for how forces, and the resulting atomic motion along a reaction coordinate, originate from a nonequilibrium population of excited electronic states. Using femtosecond photoemission, we obtain access to the transient electronic structure during an ultrafast PIPT in a model system: indium nanowires on a silicon(111) surface. We uncover a detailed reaction pathway, allowing a direct comparison with the dynamics predicted by ab initio simulations. This further reveals the crucial role played by localized photoholes in shaping the potential energy landscape and enables a combined momentum- and real-space description of PIPTs, including the ultrafast formation of chemical bonds.

Reactive events in nature are associated with the formation or breaking of chemical bonds. Within the Born-Oppenheimer approximation (*1*), a description of reactions that separates the atomic and electronic degrees of freedom is used, such that the atomic system evolves across a potential energy surface defined by the transient electronic structure. To test the validity of this nonequilibrium approach, whether in finite or extended systems, requires knowledge of both atomic and electronic structure on ultrafast time scales. The ultrafast dynamics of insulator-to-metal phase transitions offer an especially promising route because the change in electronic structure during these events is particularly extreme, and typically accompanied by a structural distortion. Ultrafast techniques have opened up avenues for exploring the interplay between the atomic and electronic subsystems (*2*–*5*), including during photoinduced insulator-to-metal transitions (*6*–*9*); these techniques additionally enabled the making of reciprocal space movies charting electronic structure dynamics (*7*, *10*) and "molecular movies" (*4*, *11*), which follow the real-time position of atoms during structural changes. Uniting these concepts to examine not only atomic positions, but also the underlying electronic structure determining the reaction pathway along the potential energy surface (PES), has been a long-pursued goal (*12*). Time- and angle-resolved photoemission spectroscopy (trARPES) is ideally suited for accessing the nonequilibrium electronic structure, as it allows direct access to the electronic band structure on ultrafast time scales and its occupation in momentum space ($\boldsymbol{k}$). Furthermore, this picture of electronic bands in periodic systems, often favored by physicists, is Fourier-equivalent to a real-space ($\boldsymbol{r}$) description of chemical bonds (*13*, *14*), which suggests the possibility of following ultrafast bond dynamics in $\boldsymbol{r}$-space (*15*) based on measurements in $\boldsymbol{k}$-space (*16*). We realize this by determining the reaction pathway—including the full electronic structure dynamics—during an ultrafast structural phase transition at a surface, thereby going beyond the molecular movie concept.

Our model phase transition system consists of atomic indium nanowires on the (111) surface of silicon, denoted In/Si(111). The system undergoes an order-order structural transition accompanied by an electronic insulator-to-metal transition (*17*, *18*). A close interplay between the electronic structure and specific lattice motions during the phase transition has been predicted that, in addition to a detailed knowledge of the equilibrium structure (*19*–*21*), makes this system ideal for investigating ultrafast changes in both $\boldsymbol{k}$- and $\boldsymbol{r}$-space. Recent time-resolved electron diffraction measurements have revealed that the structural photoinduced phase transition (PIPT) is completed within 1 ps (*22*), but such a technique does not give direct access to the underlying transient electronic dynamics.

Here we use trARPES to follow the ultrafast evolution of the electronic band structure during the PIPT in In/Si(111), which, combined with ab initio molecular dynamics (AIMD) simulations, allows access to the microscopic forces and mechanisms driving the structural transition and the dynamics of chemical bonds. To measure the dynamics of the electronic structure of In/Si(111), we have developed a 500-kHz repetition rate extreme ultraviolet (XUV) source at 22 eV (*23*), representing a substantial advance compared with the state of the art (*24*, *25*). This allows efficient access to the full, or even multiple, Brillouin zones (BZs) in many materials. A schematic trARPES experiment is shown in Fig. 1A: The pump pulse ($h\nu$ = 1.55 eV) excites electrons above the Fermi level (E_F); the electrons are then ejected from the sample after a variable delay time Δt by the probe pulse ($h\nu$ = 22 eV). A cross-correlation of 40 fs between pump and probe pulses is obtained. In contrast to traditional ARPES (*26*), this allows simultaneous access to the electronic structure above and below E_F (Fig. 1B).

In/Si(111) undergoes a transition from an insulating (8 × 2) to a metallic (4 × 1) structure above 130 K (*27*, *28*) (Fig. 1, C and D). The bonding motif in the insulating phase (Fig. 1C) consists of distorted hexagons, whereas in the conducting phase, the In atoms rearrange into zig-zagging chains (Fig. 1D). The $\boldsymbol{k}$-space band structures of the two phases calculated within the *GW* approximation are given in Fig. 1, E and F. In contrast to the (4 × 1) phase, which has three metallic bands (m_1 to m_3) that cross E_F (*17*) (Fig. 1F), the (8 × 2) phase is gapped at the $\bar{\Gamma}_{8\times2}$ and $\bar{X}_{8\times2}$ points (Fig. 1E). Upon increasing the temperature across the (8 × 2) to (4 × 1) phase transition, the states initially lying far above E_F at $\bar{\Gamma}_{8\times2}$ shift down in energy and eventually cross E_F, forming the metallic m_1 band of the (4 × 1) phase. Concurrently the energy gap in the m_2 and m_3 bands at the $\bar{X}_{8\times2}$ point closes, and the bands shift apart in momentum along the k_x direction (*23*). We note that the three metallic bands predicted from the calculation in the (4 × 1) phase are clearly observed in Fig. 1B. The Fermi surface of the (4 × 1) phase in Fig. 1G shows the momentum cut along which our data are obtained.

To investigate the PIPT, we cooled the sample to 25 K and photoexcited it by a pump pulse with incident fluence F = 1.35 mJ cm^{-2}, which corresponds to an excitation density in the surface In layer of around one electron per unit cell, implying a homogeneous excitation far from a dilute limit. Selected snapshots following excitation are shown in Fig. 2, A to D. At Δt = −450 fs (Fig. 2A), the XUV pulse arrives before the pump pulse; hence, the band structure reflects the unperturbed (8 × 2) phase with only states below E_F occupied. Shortly after excitation, at Δt = 50 fs (Fig. 2B), previously unoccupied states above E_F become clearly visible. An evolution of electronic states occurs, most clearly observed for the states around $\bar{\Gamma}_{8\times2}$ (k_x = 0.75 Å^{-1}), which shift down in energy between Δt = 50 and Δt = 250 fs (Fig. 2C). At Δt = 900 fs (Fig. 2D), the system has fully transformed into the (4 × 1) phase. The overlaid *GW* band structure for the two phases highlights the occurrence of the PIPT.

The dynamics of selected spectral features chart the progress of the PIPT (Fig. 2E). The arrows in Fig. 2, A to D, mark the positions and the direction along which one-dimensional slices of the data are analyzed and fitted to obtain the band positions presented in Fig. 2E as a function of time delay [see also (*23*)]. The fastest dynamics are found at $\bar{X}_{8\times2}$ (red arrow in Fig. 2A), where the band gap closes within 200 fs, thus defining the ultrafast insulator-to-metal transition. As a second step, the conduction band edge at the BZ

[1]Department of Physical Chemistry, Fritz-Haber-Institut der Max-Planck-Gesellschaft, Faradayweg 4-6, 14195 Berlin, Germany. [2]Department of Physics, University of Paderborn, Warburger Strasse 100, 33098 Paderborn, Germany.
***Corresponding author. Email: christopher.nicholson@unifr.ch (C.W.N.); wolf@fhi-berlin.mpg.de (M.W.)**
†Present address: Department of Physics, University of Fribourg, Chemin du Musée 3, 1700 Fribourg, Switzerland.

zone center (orange arrow) is found to reach E_F after 500 fs. Finally, the structural transition, as measured by the splitting between bands m_2, m_3 (Fig. 2D, blue arrows), is completed after ~700 fs. This third time scale is in excellent agreement with the structural transition time scale observed by time-resolved electron diffraction, which is completed after ~700 fs with a time constant τ = 350 fs (*22*). It is notable that even before the structural transition is completed, two physically meaningful electronic transitions have occurred.

The distinct time scales of these three spectral features reveal a detailed pathway of the phase transition as it evolves along the electronic PES. To gain microscopic insight into the evolution of the atomic structure, electronic properties, and bond strengths along this pathway, we have performed AIMD simulations based on density functional theory (DFT) within the local density approximation (LDA), constrained by the experimental results. Because the experiment reveals the transient changes to the electronic states and their occupation, these can be used to simulate realistic excitation scenarios with AIMD. We have mapped the experimental ***k***-space distribution of excited carriers across multiple BZs in Fig. 3. This reveals that electrons are strongly delocalized throughout the BZ, in contrast to photoholes, which are localized at the BZ boundary. Such a distribution is substantially different from that of the excitation conditions assumed in a previous study, which forced excited electrons to be confined to the BZ center (*22*). In a first attempt, we assume transiently hot electronic distributions in the AIMD simulations based on the

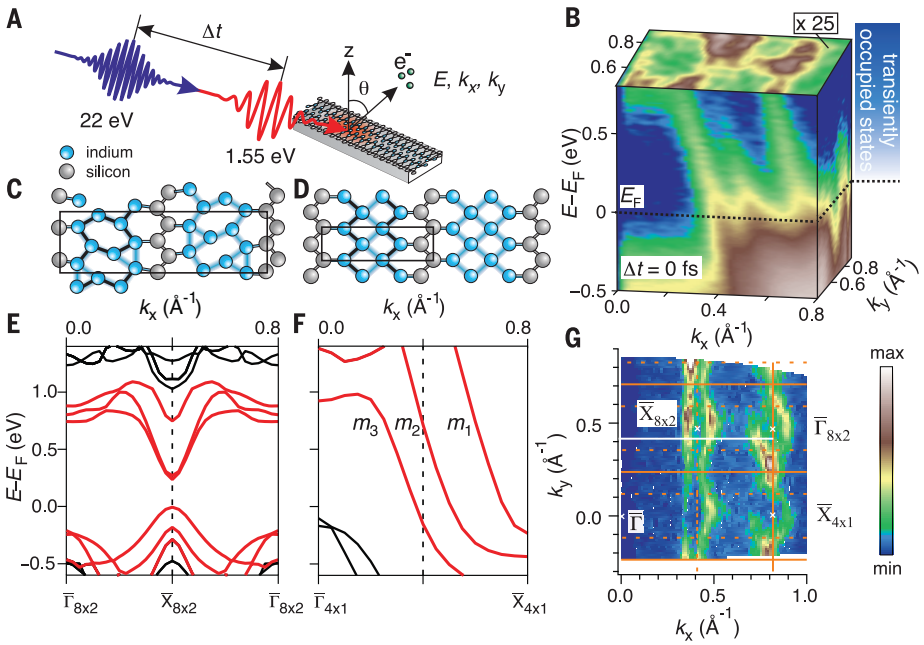

Fig. 1. Experiment overview and material system. (**A**) Schematic trARPES experiment, where Δt is the variable delay between pump (red) and probe (purple) pulses. (**B**) Excited-state photoemission data (log-color scale) obtained at T = 150 K in the metallic (4 × 1) phase with an excitation fluence F = 2 mJ cm^{-2}. (**C**) Schematic ***r***-space structure in the (8 × 2) phase and (**D**) in the (4 × 1) phase. Solid black lines highlight the structural motifs of the two phases, blue lines represent bonds. (**E**) Electronic band structure (***k***-space) calculated within the *GW* approximation in the (8 × 2) phase and in (**F**) for the (4 × 1) phase, corresponding to the structures in (C) and (D). The experimental characterization of the two phases is shown in (*23*). (**G**) Fermi surface obtained at 150 K with the 22-eV laser revealing the cut along which time-resolved measurements were obtained (white line). Solid orange lines mark the (4 × 1) BZ boundaries, whereas dashed lines mark the boundaries of the (8 × 2) BZ. High-symmetry points in the two phases are marked with crosses.

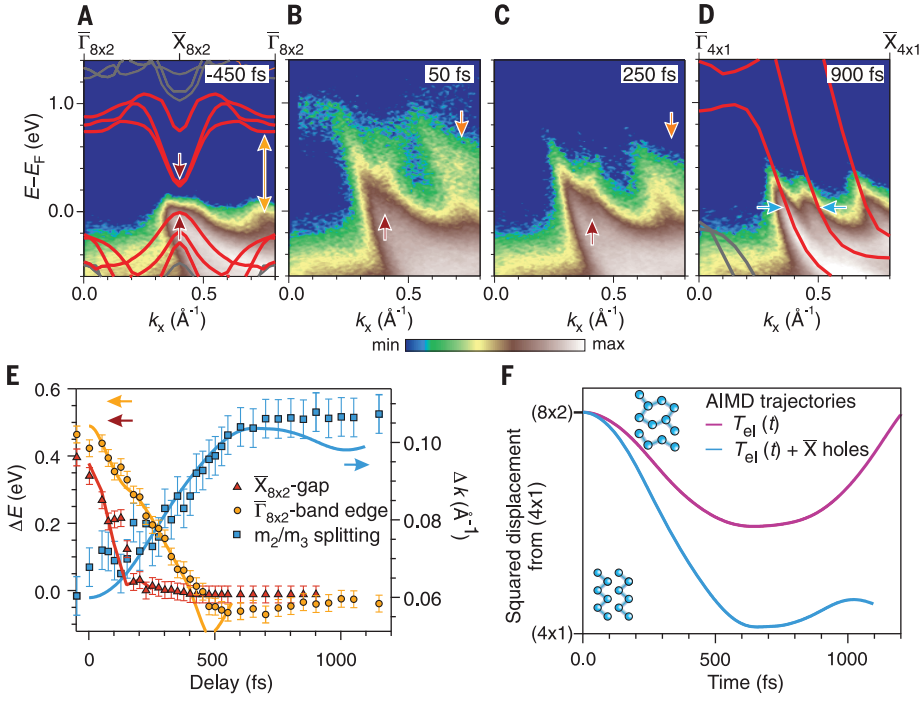

Fig. 2. Electronic and atomic structure during photoinduced phase transition. (**A** to **D**) trARPES data (F = 1.35 mJ cm^{-2}) on a logarithmic color scale at selected delays at a base temperature of T = 25 K. Arrows highlight the positions of the features of interest, which are followed in (E). (**E**) Dynamics of the features marked by arrows in (A) and (D). Red data points track the size of the band gap at the zone boundary over time, whereas the orange data mark the position of the band edge at the zone center with respect to the Fermi level. The blue data reveals the change of splitting between the two innermost bands marked in (D). Solid curves are the dynamics of the relevant spectral features from AIMD simulations, rescaled with respect to the GW band structure. For further details, see (*23*). (**F**) Evolution of the atomic structure (AIMD trajectories) through the PIPT, showing the mean squared displacement of the atomic positions from the (4 × 1) phase following excitation: $\sum_i |R_i - R_{i,4\times1}|^2$. Trajectories for two initial excitation conditions are shown, including (blue) and not including (purple) the observed localized hole population; only the former drives the PIPT. During the PIPT, the relevant atomic modes evolve with an average speed of 0.1 pm fs^{-1} (*23*).

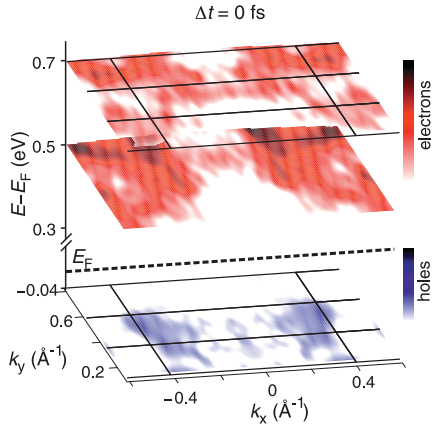

Fig. 3. *k*-space distribution of excited carriers. Experimentally measured difference map of the photoemission signal throughout multiple BZs in the (8 × 2) phase, revealing the distribution of excited electrons (red) and holes (blue) following photoexcitation (F = 0.7 mJ cm^{-2}). The distribution is obtained from the difference between spectra before excitation (Δt = −1000 fs) and Δt = 0 fs.

experimentally determined time-dependent electronic temperature (fig. S6). However, the corresponding calculated trajectory (purple curve in Fig. 2F) describes an incomplete phase transition: The system starts to evolve from the (8 × 2) phase toward the (4 × 1) phase, but finally returns to the (8 × 2) ground state. This indicates that the LDA-DFT electronic structure is not sufficiently accurate. Indeed, the inclusion of electronic self-energy effects within the *GW* approximation raises the energy of the uppermost zone boundary valence state by about 0.2 eV with respect to the zone center states (fig. S7). Self-energy effects beyond the LDA thus lead to the preferential confinement of photoholes at the BZ boundary as experimentally observed (Fig. 3). Unfortunately, AIMD simulations based on a self-energy corrected electronic structure are computationally prohibitively expensive. Therefore, we compensate the misalignment of the valence state energies on an ad hoc basis by fixing the occupation numbers (on top of the thermal occupation) in the AIMD simulations such that holes occur at the BZ boundary and the zone center valence states are occupied (*23*). The AIMD simulation based on this excitation scenario now indeed results in a complete phase transition (Fig. 2F, blue curve). This underlines the role of zone-boundary photoholes as a key driving force in the structural transition. Moreover, the corrected AIMD simulation reproduces all three time scales observed in the ***k***-space experiment (Fig. 2E, solid lines), revealing a high level of accuracy in the simulated PES and the corresponding trajectory, even on these ultrafast time scales. The excellent agreement between our data and the simulations is strong evidence for the coherent directed motion of atoms within all unit cells during the PIPT, in accord with the previous electron diffraction study (*22*). Such ultrafast directed dynamics cannot

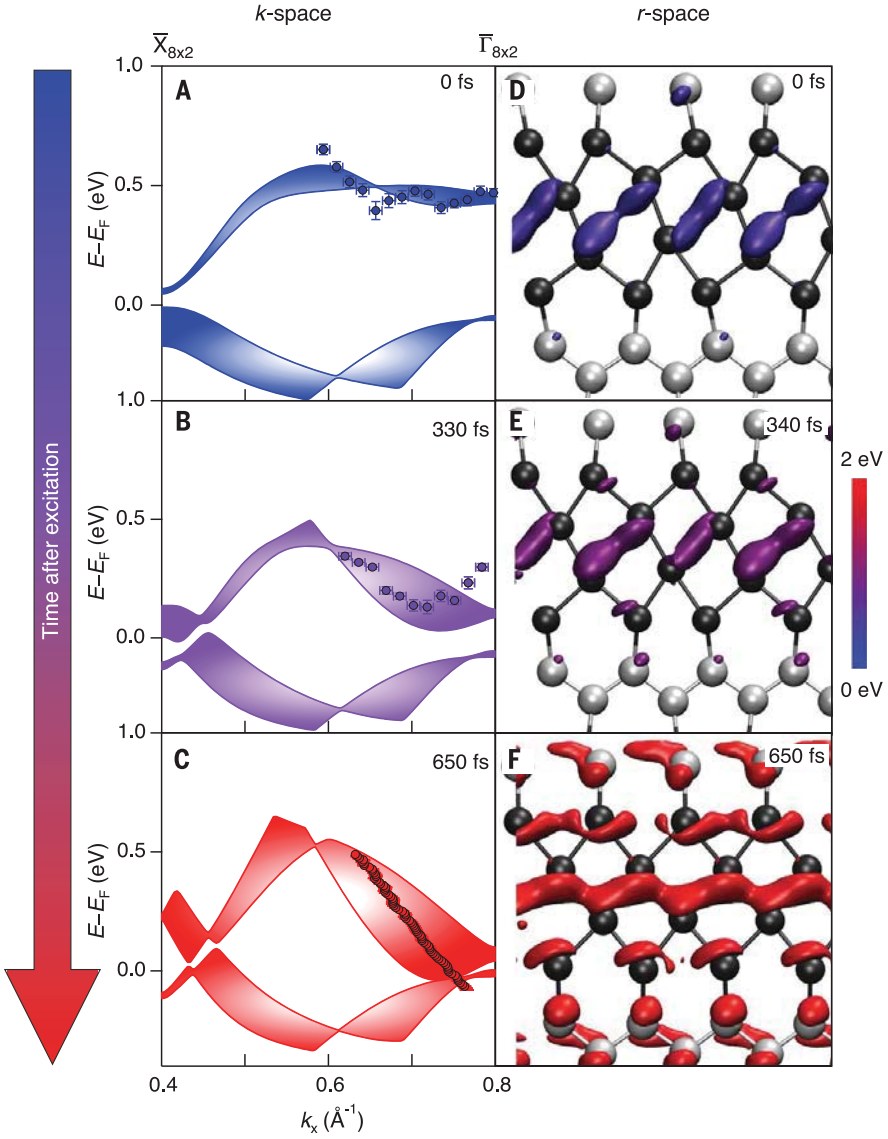

Fig. 4. Dynamics of bands and bonds during the insulator-to-metal transition. (**A** to **C**) Position of the ***k***-space bands close to the $\bar{\Gamma}_{8\times2}$ point at selected time delays extracted from the trARPES data, overlaid on the calculated LDA band structure (color-filled for clarity). Error bars mark a 95% confidence level. (**D** to **F**) Corresponding ***r***-space dynamics of the orbital, obtained from the Fourier transform of the ***k***-space band structures associated with the $\bar{\Gamma}_{8\times2}$ band in (A) to (C). Both the shape of the orbital distribution and the bond strength—indicated by the color scale—change during the phase transition, as a bond across the indium hexagon is formed. A complementary picture of charge transfer during the bond formation and breaking, as well as movies of the full ***k***- and ***r***-space dynamics (movies S1 and S2), can be found in (*23*).

be explained by a statistical picture of the phase transition where different regions of the sample evolve incoherently (*23*).

To further exemplify the high level of agreement between experiment and theory, in Fig. 4, A to C, we compare the calculated band structure at three snapshots during the PIPT with the corresponding band position at $\bar{\Gamma}_{8\times2}$ extracted from our data. Both the calculated energetic position and the slope of the dispersion are observed to change in agreement with the experimental data. This agreement enables us to extract the ***r***-space dynamics of nuclei and chemical bonds during the PIPT from the simulation. To do so, we plot the electronic orbitals associated with the bands discussed above at the BZ center ($\bar{\Gamma}_{8\times2}$) in Fig. 4, D to F, again for three snapshots. A transition from an orbital localized between opposite In hexagon atoms to a delocalized metallic state along the In chains is clearly seen during the PIPT.

To describe chemical bond formation additionally requires a measure of the bond strength. A quantitative understanding of bond strengths in extended systems can be gained from the crystal overlap Hamiltonian population (COHP)

(*29*, *30*), which resolves each band into bonding and antibonding contributions as a function of energy—essentially a bonding character density of states for each electronic band. By performing a COHP analysis along the AIMD trajectory, we obtain the evolution of the surface bond strengths during the phase transition (*23*). In Fig. 4, D to F, we show the formation of an In-In bond across the neighboring chains. A gradual evolution of the bond strength up to 2 eV is observed, encoded in the blue-to-red color scale applied to the orbitals in Fig. 4, D to F. Combined with the orbital distribution, this reveals the ultrafast formation of an In-In bond during the transition into the (4 × 1) structure, on the same time scale as the closing of the electronic gap in this region, i.e., within 500 fs. The buildup of bond strength thus parallels the transition from a localized molecular orbital (insulator) to a delocalized (metallic) state during the phase transition.

From our analysis, the following complete microscopic mechanism for the PIPT emerges: Upon excitation, holes are created in the bonding states at $\bar{X}_{8\times2}$, which correspond to In-In dimer bonds between the outer In chain atoms (*23*). Consequently, the dimer bonds characteristic for the hexagon structure weaken and break. At the same time, a sizable fraction of excited electrons populates the states at $\bar{\Gamma}_{8\times2}$ that are formed by a bonding combination of In states from neighboring In chains. Population of these excited states leads to interatomic forces that transform the hexagons into zig-zag chains, resulting in bond formation (Fig. 4, D to F). The electron band related to these bonds (m_1) is lowered in energy as the In atoms contributing to this bond approach each other, further populating those states and strengthening the bond. It finally crosses the Fermi energy as shown in Fig. 4C, resulting in the metallic state of the (4 × 1) phase.

Our combined experimental and theoretical approach extends the molecular movie concept by revealing the ultrafast electronic structure dynamics that govern a nonequilibrium structural transition. This unifying description bridges two fundamental concepts of physics and chemistry—band structure and chemical bonds—during ultrafast reactions. Besides elucidating the effect of the nonequilibrium electronic structure on structural dynamics, understanding the potential energy landscape induced by excitation paves the way for reaction pathways engineered via tailored excitation, potentially allowing optical control over such dynamic processes.

REFERENCES AND NOTES

1. M. Born, J. R. Oppenheimer, *Ann. Phys.* **389**, 457–484 (1927).
2. H. Petek, M. J. Weida, H. Nagano, S. Ogawa, *Science* **288**, 1402–1404 (2000).
3. H. Öström *et al.*, *Science* **347**, 978–982 (2015).
4. T. Ishikawa *et al.*, *Science* **350**, 1501–1505 (2015).
5. S. Gerber *et al.*, *Science* **357**, 71–75 (2017).
6. D. Wegkamp, J. Stähler, *Prog. Surf. Sci.* **90**, 464–502 (2015).
7. F. Schmitt *et al.*, *Science* **321**, 1649–1652 (2008).
8. T. Rohwer *et al.*, *Nature* **471**, 490–493 (2011).
9. C. Monney *et al.*, *Phys. Rev. B* **94**, 165165 (2016).
10. X. Cui *et al.*, *Nat. Phys.* **10**, 505–509 (2014).
11. J. R. Dwyer *et al.*, *Philos. Trans. A. Math. Phys. Eng. Sci.* **364**, 741–778 (2006).
12. J. C. Polanyi, A. H. Zewail, *Acc. Chem. Res.* **28**, 119–132 (1995).
13. Ashcroft, N. W. & Mermin, N. D. *Solid State Physics*. (Brooks/Cole, 1976).
14. R. Hoffmann, *Rev. Mod. Phys.* **60**, 601–628 (1988).
15. T. L. Cocker, D. Peller, P. Yu, J. Repp, R. Huber, *Nature* **539**, 263–267 (2016).
16. P. Puschnig *et al.*, *Science* **326**, 702–706 (2009).
17. H. Yeom *et al.*, *Phys. Rev. Lett.* **82**, 4898–4901 (1999).
18. P. C. Snijders, H. H. Weitering, *Rev. Mod. Phys.* **82**, 307–329 (2010).
19. C. González, J. Ortega, F. Flores, *New J. Phys.* **7**, 100 (2005).
20. S. Wippermann, W. G. Schmidt, *Phys. Rev. Lett.* **105**, 126102 (2010).
21. E. Jeckelmann, S. Sanna, W. G. Schmidt, E. Speiser, N. Esser, *Phys. Rev. B* **93**, 241407 (2016).
22. T. Frigge *et al.*, *Nature* **544**, 207–211 (2017).
23. Further details are available in the supplementary materials.
24. C. M. Heyl, J. Güdde, A. L'Huiller, U. Höfer, *J. Phys. At. Mol. Opt. Phys.* **45**, 074020 (2012).
25. H. Wang *et al.*, *Nat. Commun.* **6**, 7459 (2015).
26. S. Hüfner, *Photoelectron Spectroscopy: Principles and Applications* (Springer, 1995).
27. T. Tanikawa, I. Matsuda, T. Kanagawa, S. Hasegawa, *Phys. Rev. Lett.* **93**, 016801 (2004).
28. Y. Sun *et al.*, *Phys. Rev. B* **77**, 125115 (2008).
29. R. Dronskowski, P. E. Blöchl, *J. Phys. Chem.* **97**, 8617–8624 (1993).
30. S. Maintz, V. L. Deringer, A. L. Tchougréeff, R. Dronskowski, *J. Comput. Chem.* **34**, 2557–2567 (2013).

ACKNOWLEDGMENTS

We thank P. Kirchmann, C. Monney, and Y. Deng for their contributions to developing the infrastructure of the trARPES experiment. **Funding:** We gratefully acknowledge funding from the Max-Planck-Gesellschaft and the Deutsche Forschungsgemeinschaft through FOR1700 and TRR142. The Paderborn Center for Parallel Computing (PC^2) and the Höchstleistungs-Rechenzentrum Stuttgart (HLRS) are acknowledged for grants of high-performance computer time. **Author contributions:** C.W.N. prepared and characterized the samples. C.W.N., M.P., and L.R obtained the experimental data. C.W.N. analyzed the data. A.L. and W.G.S. performed the electronic structure calculations. W.G.S., R.E., and M.W. provided the project infrastructure. All authors discussed the results and their interpretation. C.W.N. wrote the manuscript with input and discussion from all authors. R.E. and M.W. were responsible for the overall project planning and direction. **Competing interests:** The authors declare no competing interests. **Data and materials availability:** The data that underpin the findings of this study are available at https://edmond.mpdl.mpg.de/imeji/collection/ph48BTv9YHGw49oc